Likely *PKS-PKP* from Array Processing of Noise Records

Tianze Liu[1], **Peter M. Shearer**[1]

[1]Institute of Geophysics and Planetary Physics, Scripps Institution of Oceanography, UC San Diego

Key Points:

- *PKS-PKP* is retrieved from cross-component cross-correlation of seismic noise.
- *PKS-PKP* signals are enhanced by using only the time windows with strong *PKP* energy.
- *PKS-PKP* signals are enhanced by performing array stacking before cross-correlation.

Corresponding author: Tianze Liu, tianzeliu@ucsd.edu

Abstract

Seismic noise has been widely used to image Earth's structure in the past decades as a powerful supplement to earthquake signals. Although the seismic noise field contains both surface-wave and body-wave components, most previous studies have focused on surface waves due to their large amplitudes. Here, we use array analyses to identify body-wave noise traveling as *PKP* waves. We find that by cross-correlating the array-stacked horizontal- and vertical-component data in the time windows containing the *PKP* noise signals, we extract a phase likely representing *PKS-PKP*. This phase can potentially be used for shear-wave splitting analysis and studying core-mantle boundary structure. Our results also suggest that the sources of body-wave noise are extremely heterogeneous in both space and time, which should be accounted for in future studies using body-wave noise to image Earth structure.

Plain Language Summary

Seismic noise is the vibration of Earth generated by activities other than earthquakes, such as wind and ocean waves. Signals extracted from seismic noise can be used to study Earth's interior structure in ways similar to how earthquake records have been analyzed. Most previous studies using seismic noise to study Earth structure used its surface-wave component, i.e., the waves propagating at Earth's surface, whereas the body-wave component, i.e., the waves traveling through Earth's interior, is less used because body-wave noise is usually much weaker than surface-wave noise. Here, we use data collected by a dense seismic array to identify body-wave noise propagating as *PKP* waves, P waves that travel through Earth's core. We also find that a seismic phase, likely *PKS-PKP*, the P-to-S converted waves at the core-mantle boundary, can be extracted from the records of time windows containing strong *PKP* energy. This phase can potentially be used to study the anisotropic properties of Earth's crust and mantle and the structure of the core-mantle boundary.

1 Introduction

Recent decades saw a rapid expansion of studies using seismic noise to image Earth structure (e.g. Shapiro et al. (2005), Bensen et al. (2007), Brenguier et al. (2008), Lin et al. (2009), Poli et al. (2012), Nakata et al. (2015)). Most of these studies focused on extracting surface-wave signals from the noise field because surface waves usually dom-

inate the signals retrieved by noise cross-correlation. This observation is commonly attributed to the prominence of surface waves in Earth's noise field as a result of noise sources, such as wind and ocean waves, occurring mostly at the surface. Despite their lower amplitudes, body-wave signals have occasionally been retrieved from noise cross-correlations and used to image Earth structure (e.g. Poli et al. (2012), Nakata et al. (2015), Feng et al. (2021)). A major advantage of body waves over surface waves in studying Earth structure is that body-wave reflected and converted phases are sensitive to material discontinuities in Earth's interior (e.g., the Moho and the core-mantle boundary (CMB)), which cannot be resolved with surface-wave data alone. However, body-wave reflection and conversion signals are weaker than direct phases and thus more difficult to observe in the cross-correlation functions, which are typically nosier than earthquake recordings. Therefore, techniques capable of enhancing body-wave reflection and conversion signals are needed to better image Earth's discontinuities with noise records.

In addition to imaging using seismic noise, in recent years major advances have been made in understanding the sources of Earth's noise field (e.g., Gualtieri et al. (2014), Nishida and Takagi (2016), Liu et al. (2020), Retailleau and Gualtieri (2021)). Many contributions were made by studying body-wave noise signals with array techniques (e.g., beamforming and back-projection), which suggests that weak body-wave noise signals can be enhanced with array processing to better image Earth structure. These studies also showed that body-wave noise sources, which are usually associated with storms in the oceans, are likely spatially and temporally heterogeneous, which implies that body-wave signals could be better retrieved through seismic interferometry if the variations of the body-wave noise sources are properly accounted for.

Here, we present observations of body-wave noise propagating as *PKP* using data collected by a dense broadband seismic array in the central US. We further show that a phase likely representing *PKS-PKP* can be extracted by cross-correlating the array-stacked horizontal- and vertical-component noise records in the time windows containing the *PKP* noise signals. We then discuss the potential applications of this seismic phase and the implications of our findings for seismic interferometry.

2 Data and preprocessing

We mainly use the continuous data collected by the Ozark Illinois Indiana Kentucky (OIINK) Flexible Array Experiment (network code: XO), a dense 2D broadband seismic array with a station spacing of $\sim$ 25km located in the central US (Fig. 1). To make the resolution of our results more isotropic, we select the OIINK stations located in a 100-km radius circle and also include the Transportable-Array stations in this range (Fig. 1b). Although the two arrays together span 2011–2015, to ensure a reasonable resolution we focused on time windows with more than 20 active stations, which limits our analysis to a roughly one-year period between June 2012 and August 2013. We downloaded the continuous data from the IRIS Data Management Center in one-hour time time windows, removed the instrument response, and band-pass filtered the data to 2–10 seconds, which contains the secondary microseism energy (Retailleau & Gualtieri, 2021). To avoid the effects of earthquakes and instrument malfunctions, we removed the 1-hour time windows containing the first arrivals of global earthquakes with magnitude > 5 and those containing amplitudes $>1 \times 10^{-5}\,\mathrm{m\,s^{-1}}$.

3 *PKP* signals from beamforming analysis

We performed conventional linear beamforming with all three components (vertical, east, and north) of our array data to characterize the directional properties of the noise field. To save computational cost, we first performed a reconnaissance analysis over the slowness range $\pm 0.2\,\mathrm{s\,km^{-1}}$ at a grid spacing of $0.013\,\mathrm{s\,km^{-1}}$ in the W-E and S-N directions. The resulting vertical-component slowness images clearly show beams with slowness $<0.04\,\mathrm{s\,km^{-1}}$, which likely represent *PKP* signals (Fig. 2a). The horizontal-component slowness images also show local maxima corresponding to the *PKP* beams on the vertical component, though the background noise is significantly higher on the horizontal-component images (Fig. 2a), which could be due to the near-vertical particle motion of *PKP* or a more homogeneous distribution of horizontal-component noise sources. The slowness images of some time windows also show multiple peaks (e.g., 2013-07-06-00-00-00; Fig. 2a).

For seismic imaging, we prefer to use time windows dominated by *PKP* energy from a single direction because this resembles that of earthquake sources, which may make techniques in earthquake imaging readily applicable. To identify these time windows, we

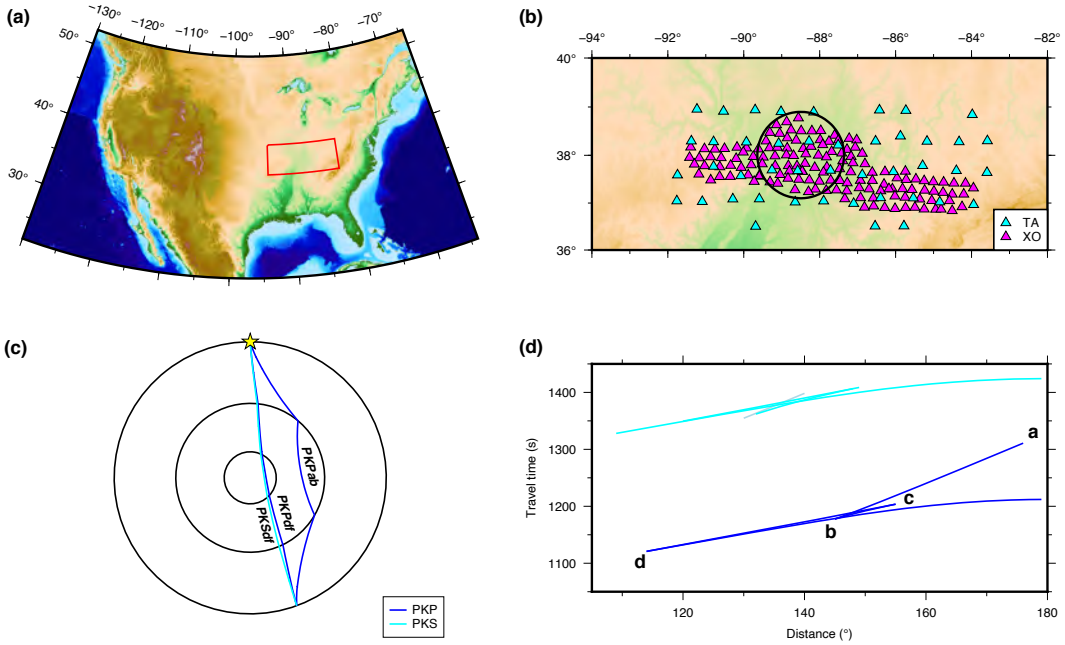

Figure 1. Station locations and *PKP* and *PKS* ray geometries and travel times. (a) Map of the contiguous US showing the closeup of panel (b) marked in red. (b) Map of all the OIINK stations (magenta) and nearby TA stations (cyan). The 100-km radius circle defines the region in which the stations are included in our analysis. (c) Ray paths of *PKPab*, *PKPdf* (blue), and *PKSdf* (cyan) at 160°. (d) Travel times as functions of epicentral distance for different branches of *PKP* (blue) and *PKS* (cyan)

find the maximum in the *PKP* range (slowness $<0.04\,\mathrm{s\,km^{-1}}$) of each vertical-component slowness image and the corresponding slowness vector, which we refer to as the *PKP* slowness. We then define the vertical-component normalized *PKP*-beam amplitude as the ratio between the maximum amplitude in the *PKP* range and the average amplitude of the whole slowness image, which measures the power of the strongest *PKP* beam relative to the background noise. We further define the corresponding normalized *PKP*-beam amplitudes for the horizontal components as the ratios between the amplitudes at the *PKP* slowness and the average amplitudes of the whole slowness images. We finally define the three-component normalized *PKP*-beam amplitude (hereafter "*PKP*-beam amplitude") as the product of the normalized *PKP*-beam amplitudes for the three components. We regard the time windows with *PKP*-beam amplitude > 2, which account for about 10% of all the time windows, as windows dominated by *PKP* energy from a single direction and make a histogram of the *PKP* slowness of these time windows, which shows that the vast majority of these time windows have slownesses close to the b and c caustics of *PKP* (Fig. 2b). This phenomenon is probably due to the amplification of *PKP* near the caustics.

To identify the source locations of these *PKP* beams, we performed beamforming for the vertical-component records of the previously identified time windows with *PKP* amplitude > 2 in the range $\pm 0.05\,\mathrm{s\,km^{-1}}$, using a finer slowness grid spacing of $0.0032\,\mathrm{s\,km^{-1}}$. We then convert these high-resolution *PKP* slowness vectors to source locations using the *PKP* slowness-distance relation computed with the IASP91 earth model (Fig. 3a, b; Kennett et al. (1995)). When different time windows have the same *PKP* slowness vector, we regard them as having the same source locations and record their cumulative duration (number of hours; Fig. 3a, b), which is sufficient for a preliminary characterization of these sources. We note that these estimated source locations are only approximate, as the slowness peaks are relatively broad in our images, 3D heterogeneity likely introduces deviations between observed slownesses and those predicted by 1D models, and the ocean-wave sources themselves are spatially defused rather than concentrated like earthquakes. A more detailed study of the spatial extent and temporal evolution of these sources will require back-projection imaging using data collected by arrays with a larger aperture than used here, which is beyond the scope of this study.

Our *PKP* sources are predominantly located in the Southern Ocean, where the ocean waves are the highest among all water bodies in the *PKP* range of our array (Fig. 3a).

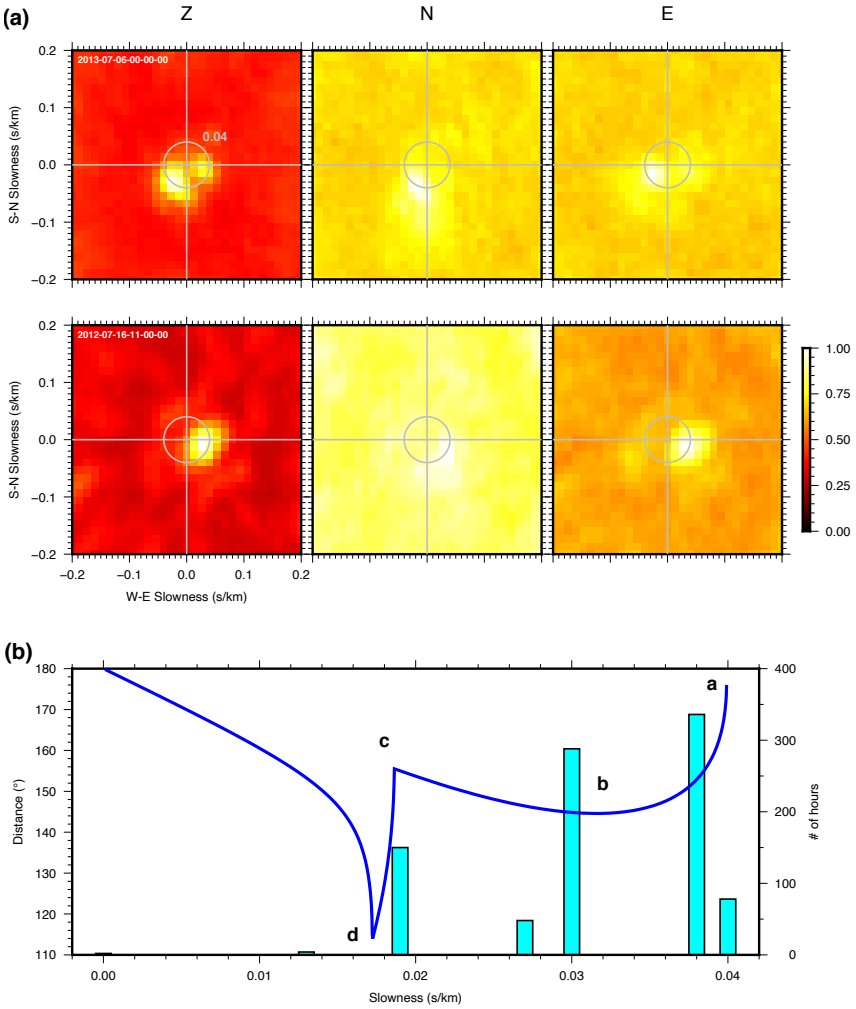

Figure 2. *PKP* beams derived with array analyses. (a) Example three-component slowness images for two one-hour time windows 2013-07-06-00-00-00 (top) and 2012-07-16-11-00-00 (bottom) with clear *PKP* energy. Gray circle: slowness of $0.04\,\mathrm{s\,km^{-1}}$. (b) Slowness-distance relation of *PKP* (blue curve) and the slowness histogram of the time windows with *PKP*-beam amplitude > 2.

We also observe far more *PKP* sources in the southern winter (Jul 2012–Sep 2012 and Apr 2013–Sep 2013) than the southern summer (Oct 2012–Mar 2013) of our observation period (Fig. 3a), which is likely due to the greater wave height in the Southern Ocean in winter. In addition to wave height, a proxy for wave energy, P-wave radiation of ocean-solid-earth interactions is also controlled by wave period and ocean depth, which can be characterized using the ocean site effect (Gualtieri et al., 2014). Our *PKP* sources appear to be mostly located in areas with high P-wave ocean site-effect at 4 and 5 s from Gualtieri et al. (2014) (Fig. 3b). The correlations between the spatial distribution of our *PKP* sources and the wave height and the ocean-site effect indicate that our *PKP* waves likely result from the nonlinear interaction of ocean gravity waves generated by storms (Gualtieri et al., 2014), consistent with the conclusions from previous studies that identified *PKP* energy in Earth's noise field (e.g. Koper and de Foy (2008), Gerstoft et al. (2008)).

We also compare the temporal variation of our *PKP* signals with global earthquake activity. Fig. 3c illustrates the variation of our *PKP*-beam amplitude over the time period of about a year, with significantly stronger *PKP* beams in southern winter than in southern summer. In addition to the broad peaks likely due to ocean activity, the *PKP*-beam amplitude shows many narrow spikes, which appear to be correlated with global seismic activity (Fig. 3c). Since the time windows containing the direct arrivals of global $M > 5$ events were removed from our analysis, these spikes must be due to the coda waves of the events, which can persist for hours after the first arrivals (Tkalčić et al., 2020). Interestingly, many of these spikes correlate with events not in the *PKP* range (gray lines in Fig. 3c), suggesting that the coda waves of global earthquakes contain waves traveling with smaller slownesses and thus steeper incident angles than the direct phases. This observation agrees with recent studies using these steeply incident coda waves to explain the phases in Earth's correlation wave field (e.g. Tkalčić et al. (2020)).

4 *PKS-PKP* from Cross-component Cross-correlation

Wave fields dominated by a single *PKP* noise source are analogous to those generated by earthquakes because the wave fields in both cases are close to unidirectional. Therefore, imaging techniques designed for earthquake data, e.g., receiver function techniques, may also be applicable to noise data dominated by a single *PKP* noise source. Here, we use cross-correlation between the horizontal- and vertical-component noise records

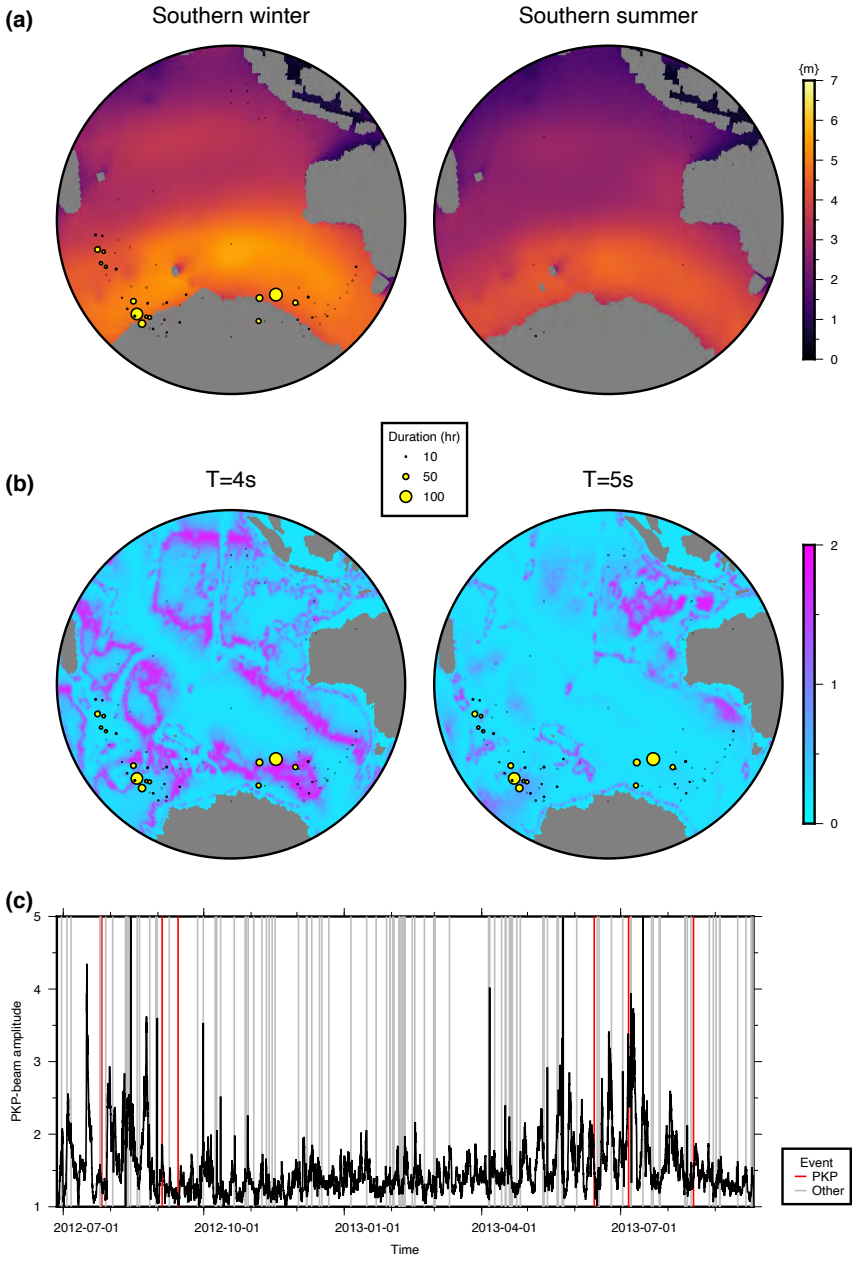

Figure 3. Spatial distribution and temporal variation of our PKP sources. (a) Spatial distributions of our *PKP* sources overlain on the ocean site-effect maps for period = 4 s (left) and 5 s (right) from Gualtieri et al. (2014). Sizes of the circles denote the cumulative duration of each source. (b) The same as (a), but for sources in the southern winter (left) and summer (right) of our observation period overlain on the average significant wave-height maps for the respective seasons from WAVEWATCH III (Tolman et al., 2009). (c) Three-component *PKP*-beam amplitude as a function of time. Red and gray lines mark the origin times of global $M > 6$ events in and out of the *PKP* epicentral distance range, respectively.

as an approximation of the deconvolution procedure in receiver-function analysis (Ammon, 1991). To enhance the near-vertically traveling *PKP* waves while reducing surface-wave energy, which typically dominates Earth's noise field, we stack the vertical- and horizontal-component records of all the active stations in the array before performing cross-correlation on the stacked records (hereafter "array stacking"). The resulting E-Z and N-Z cross-correlation functions show a clear arrival at ∼215 s, whose amplitude appears to temporally correlate with the *PKP*-beam amplitude (Fig. 4a, b). This correlation is more clearly shown when we compare the temporal variation of the relative amplitude of the 215-second phase, defined as the ratio between the average absolute amplitude in a 30-second window around 215 s and that in a 90-second window around 215 s, on daily stacked cross-correlation functions (red in Fig. 4b) with the temporal variation of the *PKP*-beam amplitude (black in Fig. 4b). This correlation suggests an association of this phase with the interaction between P waves and Earth's core. Following previous noise-imaging studies, we stacked the cross-correlation functions of many time windows to enhance the signal-noise-ratio of this phase (hereafter "215-second phase"). The results show that stacking using only the time windows with a strong *PKP* beam produces a stronger 215-second phase than stacking using both the time windows with and without strong *PKP* beams (Fig. 4c–d), which is expected because the time windows without strong *PKP* beams generally do not show a clear 215-second phase 4a, b). Hereafter, we will focus on the time windows with *PKP*-beam amplitude > 2, which likely contain the highest-quality 215-second phases (Fig. 4).

To test the effects of array stacking on the waveform quality, we computed the stacked cross-correlation functions for each station individually before stacking them. Note that the difference between this method without array stacking and the method with array stacking is whether stacking across different stations is performed after (without array stacking) or before (with array stacking) cross-correlations. The comparison between the results of these two methods clearly shows that the method with array stacking produces significantly stronger 215-second phases (Fig. 4c), which is likely because stacking the noise records across the array enhances the near-vertically traveling *PKP* noise and the associated phases, which are responsible for the 215-second phase. From now on, we will show only the results from the cross-correlation functions with array stacking.

To further characterize the 215-second phase, we binned the *PKP* slowness vectors into grids with 15° and $0.005\,\mathrm{s\,km^{-1}}$ spacing in azimuth and slowness and stacked

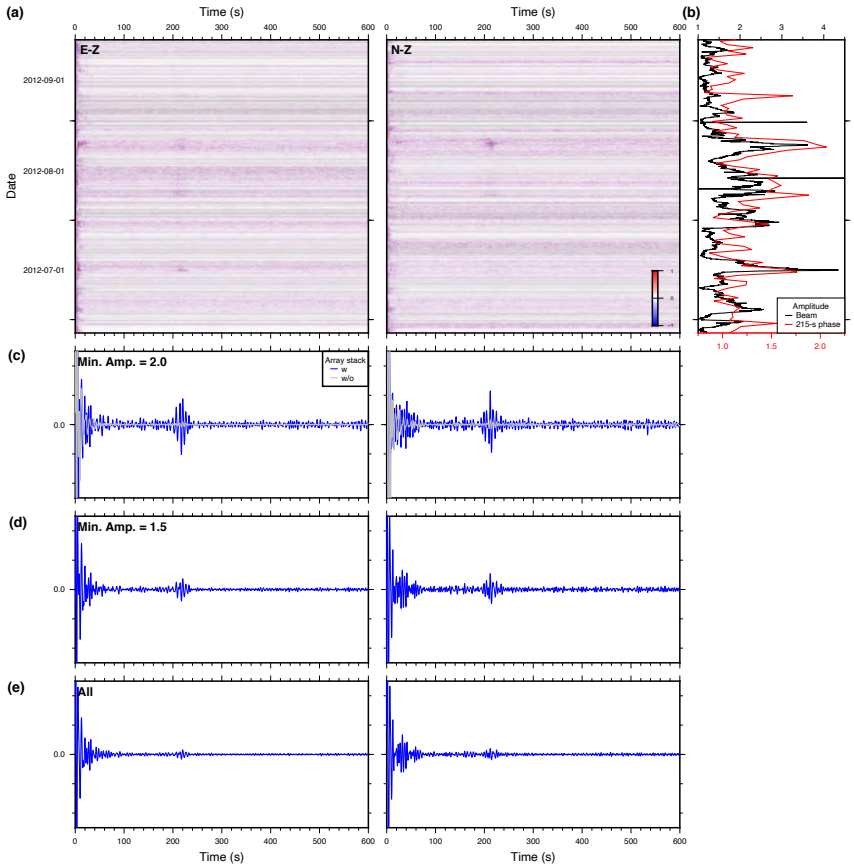

Figure 4. E-Z and N-Z cross-correlation functions of the array-stacked records. (a) E-Z (left) and N-Z (right) cross-correlation functions for all the active time windows in a three-month period from June to September 2012. (b) Temporal variation of *PKP*-beam amplitude (black) and the 215-second-phase amplitude (red) for the time range in (a). (c–d) Blue waveform: Stacked E-Z (left) and N-Z (right) cross-correlation functions for time windows with *PKP*-beam amplitude (c) > 2, (d) > 1, and (e) all the time windows. Gray waveform in (c): The same as the blue waveform, but computed with stacking E-Z and N-Z cross-correlation functions of individual stations.

the cross-correlation functions of the time windows in each bin (hereafter "*PKP*-source bin"), which is analogous to receiver-function stacks for groups of nearby earthquakes. While processing the data for each *PKP*-source bin, we aligned the records of individual stations using the back azimuth and slowness of the bin before performing array stacking, which further enhances the *PKP* signals. The stacked waveform shows that although the amplitude of the 215-second phase varies significantly across different source bins, its arrival time stays almost the same (Fig. 5). We also computed the best-fitting linear polarization direction for the 215-second arrival of each *PKP* source by finding the direction that maximizes the maximum absolute amplitude of the 215-second arrival, which is taken in a 30 s time window around 215 s, on the signal projected to the direction. These polarization directions (red bars in Fig. 5) agree very well with those of the corresponding sources bins (black bars in Fig. 5), suggesting that the 215-second phase consists of mostly SV energy.

Based on the above observations about our 215-second phase, we interpret it as *PKS-PKP* (Fig. 1c). Because travel-time curves of the same branches of *PKP* and *PKS* are almost parallel (Fig. 1d), the differential travel time of the two phases stays at ∼215 s across a broad range epicentral distance, which is consistent with the observation that our 215-second phase remains at approximately the same time for sources with different slownesses (Fig. 5). The radial polarization of our 215-second phase also agrees with that of *PKS*, which consists only of SV waves in an isotropic earth. Although different branches of *PKP* and *PKS* often arrive in the same distance range (Fig. 1c, d), the near-constant arrival time of our 215-second phase indicates that it most likely results from the cross-correlation of *PKP* and *PKS* phases from the same branch. One possible explanation for this observation is that the different ray paths of different *PKP* and *PKS* branches leave different structural imprints on their waveform, which causes them to decorrelate.

Among our *PKP* beams, many have slownesses $>0.032\,\mathrm{s\,km^{-1}}$, which suggests that they belong to the *PKPab* branch. However, *PKPab* does not coexist with *PKSab* at the same distance (Fig. 1d), which appears to suggest that their clear *PKS-PKP* signals (e.g. Fig. 5a) result from cross-correlation between *PKPab* and *PKS* of other branches. To investigate this issue, we performed beamforming using the same dataset for four earthquakes from the USGS earthquake catalog (EQ1–4) that are close to one of our *PKP* sources with slowness $>0.032\,\mathrm{s\,km^{-1}}$ (2013-07-06-00-00-00; Fig. S1). Among them, EQ1 and EQ2

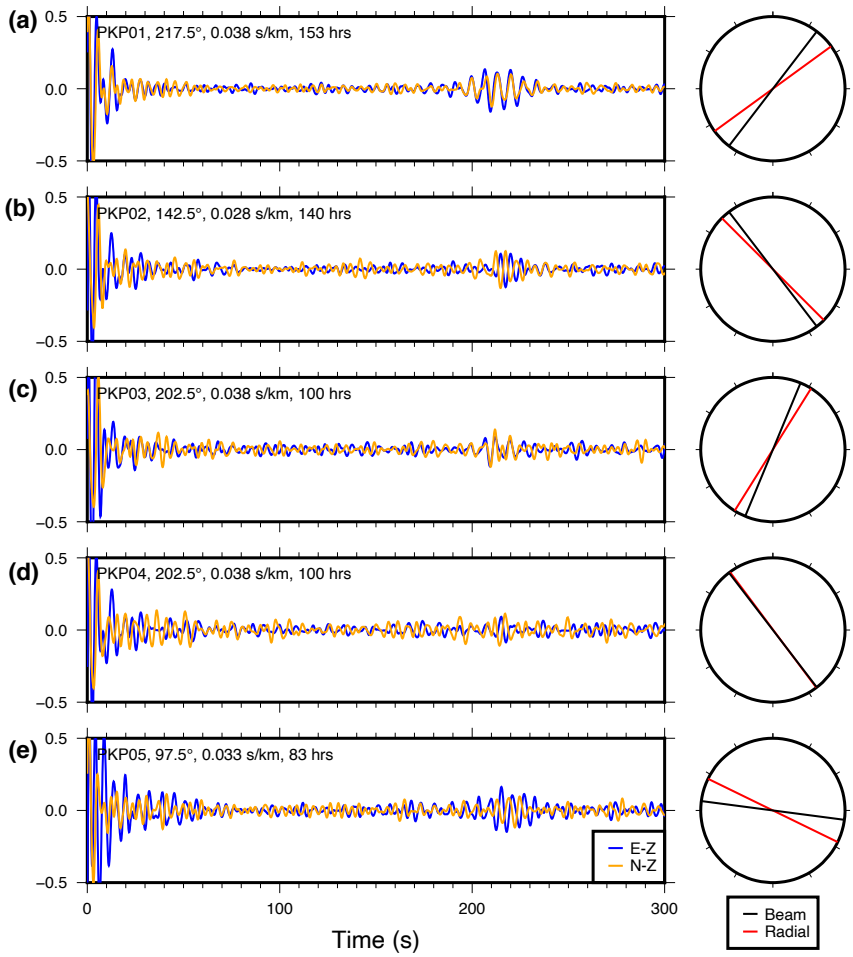

Figure 5. Stacked cross-correlation functions for the five PKP-source bins with the most cumulative duration: (a) PKP01, (b) PKP02, (c) PKP03, (d) PKP04, and (e) PKP05. Left column: Stacked E-Z (blue) and N-Z (yellow) cross-correlation functions. Right column: *PKP* beam direction (black) and the best-fit linear polarization (red) for the signals in a 30-s time window around 215 s.

show good agreement between the observed and predicted slowness, whereas EQ3 and EQ4 show greater slownesses than the predictions (Fig. S1c), which are probably due to lateral heterogeneity along the ray paths. We thus infer that our *PKP* beams with $>0.032\,\mathrm{s\,km^{-1}}$ may actually represent *PKPbc* waves whose slownesses are elevated due to similar 3D structural effects, which, unlike *PKPab*, coexist with *PKSbc* at the same distance. We note that the 3D structural effects likely also cause errors in our *PKP* source locations, which should only be regarded as preliminary estimates.

5 Discussion

To our knowledge, this is the first report of *PKS-PKP* retrieved from noise data. Although our *PKS-PKP* observation has the same arrival time ($\sim$215 s) as *cS-cP*, a phase in Earth's correlation wavefield, at zero station offset (Phạm et al., 2018), the two phases are fundamentally different for two main reasons: First, our *PKS-PKP* has its counterpart in earthquake records *PKS*, whereas *cS-cP* is not observed in earthquake records. Second, our *PKS-PKP* is extracted via cross-correlation of different data components recorded at the same location, whereas *cS-cP* is retrieved through cross-correlation of vertical-component data recorded at different locations (Phạm et al., 2018). Because *PKS* is routinely used for shear-wave-splitting analyses (e.g. Long and Silver (2009)), we also experimented with shear-wave splitting analysis (see Supplementary Text 1 for the method) using our *PKS-PKP* observations but obtained results very different from previous studies. The two *PKP*-source bins with the clearest *PKS-PKP* waveforms, PKP01 and PKP05 (Fig. 5), yielded fast directions of 121° and 127°, respectively (Figs. S2 and S3), significantly different from $\sim$70° given by shear-wave-splitting analyses of earthquake data (Yang et al., 2017). This discrepancy could be due to the low quality of our signals as the eigenvalue-ratio distributions indicate that neither of the two measurements is very conclusive (Figs. S2c and S3c). Since our data contain energy only in the narrow band between 2 and 10 s, whereas earthquake data typically contain more long-period energy, another possible explanation for this discrepancy is that our results are affected more by shallow structure than those from earthquake data. This hypothesis is supported by previous studies showing increased sensitivity of *SKS* splitting parameters to shallow structure at shorter periods (e.g. Sieminski et al. (2008)). In addition, Wirth and Long (2014) gave a NW-SE fast direction in the upper lithosphere of our study area, which is more consistent with our results.

Although the arrival time of our *PKS-PKP* observations stay mostly the same for different *PKP* sources, its amplitude varies significantly (Fig. 5). This variation does not appear to be due to stacking fold because sources with lower stacking fold can have stronger *PKS-PKP* than those with higher stacking folder (e.g. PKP05 compared with PKP04). Therefore, the variation is likely due to differences in the sources or the structures that the waves travel through. The sources with stronger *PKS-PKP* may radiate stronger *PKP* waves. Alternatively, heterogeneity at the core-mantle boundary (CMB), e.g. the Ultra Low Velocity Zones (Garnero et al., 1998), may cause changes in *PKS* waveforms. One way to separate contributions from source and structure is to observe *PKS-PKP* across a broader range. The Transportable Array (TA) is suitable for this purpose, although its station density is significantly lower than that used here. Nonetheless, we may be able to achieve a similar signal quality with the TA data by stacking stations within a broader radius (the current limit is a 100 km-radius circle) because the increased range will still be much smaller than the depth to the CMB.

Our results show that *PKP* noise sources are extremely variable in both space and time, which likely also applies to other body-wave noise sources. We also find that body-wave scattering signals extracted from noise data can be significantly enhanced with simple techniques, namely time-window selection and array stacking, that address the spatiatemporal variation of body-wave sources. In principle, time-window selection does not require dense-array data, although a synchronous array may be necessary to determine the time windows containing significant body-wave noise energy. Array stacking requires array data, which limits its application, although the required array density likely depends on the targeted seismic phase. So far, most of the seismic imaging studies using body-wave noise have not accounted for its spatiatemporal variation and have relied simply on stacking large number of cross-correlation functions (e.g. Poli et al. (2012) and Feng et al. (2021)). Our results suggest that the primary contribution to their signals may have only come from a fraction of all the time windows, and that simply selecting those time windows might significantly improve the signal quality (Fig. 4). The signal quality may be further improved if array stacking can be performed before cross-correlation.

6 Conclusions

We extract a phase that likely represents *PKS-PKP* from cross-component cross-correlation of noise recordings. We show that the amplitude of *PKS-PKP* is significantly

enhanced when only time windows containing strong *PKP* signals are used. We also show that stacking array data before cross-correlation significantly enhances *PKS-PKP* amplitudes. Future studies that retrieve body-wave scattered phases from noise data should account for the spatiatemporal variation of body-wave noise sources.

Data Availability Statement

The seismic and wave-height data used in this study are freely available through the Incorporated Research Institutions for Seismology Data Management Center (IRIS DMC) `https://ds.iris.edu/ds/nodes/dmc/` and the Environmental Modeling Center of NOAA `https://polar.ncep.noaa.gov/waves/wavewatch/`, respectively. The plots in this paper are created with the Generic Mapping Tools (Wessel et al., 2019).

Acknowledgments

This study is funded by NSF Grants EAR-1358510 and EAR-1829601. T.L. is supported by a Green Postdoctoral Scholarship. IRIS DMC is funded by the the NSF under Cooperative Support Agreement EAR-1851048. We thank Lucia Gualtieri for providing the ocean site-effect maps and Wenyuan Fan for stimulating discussion.

References

Ammon, C. J. (1991). The isolation of receiver effects from teleseismic p waveforms. *Bulletin-Seismological Society of America*, *81*(6), 2504–2510.

Bensen, G., Ritzwoller, M., Barmin, M., Levshin, A. L., Lin, F., Moschetti, M., ... Yang, Y. (2007). Processing seismic ambient noise data to obtain reliable broad-band surface wave dispersion measurements. *Geophysical Journal International*, *169*(3), 1239–1260.

Brenguier, F., Campillo, M., Hadziioannou, C., Shapiro, N. M., Nadeau, R. M., & Larose, E. (2008). Postseismic relaxation along the san andreas fault at parkfield from continuous seismological observations. *science*, *321*(5895), 1478–1481.

Feng, J., Yao, H., Wang, Y., Poli, P., & Mao, Z. (2021). Segregated oceanic crust trapped at the bottom mantle transition zone revealed from ambient noise interferometry. *Nature communications*, *12*(1), 1–8.

Garnero, E. J., Revenaugh, J., Williams, Q., Lay, T., & Kellogg, L. H. (1998). Ul-

tralow velocity zone at the core-mantle boundary. *The core-mantle boundary region*, *28*, 319–334.

Gerstoft, P., Shearer, P. M., Harmon, N., & Zhang, J. (2008). Global p, pp, and pkp wave microseisms observed from distant storms. *Geophysical Research Letters*, *35*(23).

Gualtieri, L., Stutzmann, É., Farra, V., Capdeville, Y., Schimmel, M., Ardhuin, F., & Morelli, A. (2014). Modelling the ocean site effect on seismic noise body waves. *Geophysical Journal International*, *197*(2), 1096–1106.

Kennett, B. L., Engdahl, E., & Buland, R. (1995). Constraints on seismic velocities in the earth from traveltimes. *Geophysical Journal International*, *122*(1), 108–124.

Koper, K. D., & de Foy, B. (2008). Seasonal anisotropy in short-period seismic noise recorded in south asia. *Bulletin of the Seismological Society of America*, *98*(6), 3033–3045.

Lin, F.-C., Ritzwoller, M. H., & Snieder, R. (2009). Eikonal tomography: surface wave tomography by phase front tracking across a regional broad-band seismic array. *Geophysical Journal International*, *177*(3), 1091–1110.

Liu, Q., Ni, S., Qiu, Y., Zeng, X., Zhang, B., Wang, F., ... Xu, Z. (2020). Observation of teleseismic s wave microseisms generated by typhoons in the western pacific ocean. *Geophysical Research Letters*, *47*(19), e2020GL089031.

Long, M. D., & Silver, P. G. (2009). Shear wave splitting and mantle anisotropy: Measurements, interpretations, and new directions. *Surveys in Geophysics*, *30*(4), 407–461.

Nakata, N., Chang, J. P., Lawrence, J. F., & Boué, P. (2015). Body wave extraction and tomography at long beach, california, with ambient-noise interferometry. *Journal of Geophysical Research: Solid Earth*, *120*(2), 1159–1173.

Nishida, K., & Takagi, R. (2016). Teleseismic s wave microseisms. *Science*, *353*(6302), 919–921.

Phạm, T.-S., Tkalčić, H., Sambridge, M., & Kennett, B. L. (2018). Earth's correlation wavefield: Late coda correlation. *Geophysical Research Letters*, *45*(7), 3035–3042.

Poli, P., Campillo, M., Pedersen, H., Group, L. W., et al. (2012). Body-wave imaging of earth's mantle discontinuities from ambient seismic noise. *Science*,

338(6110), 1063–1065.

Retailleau, L., & Gualtieri, L. (2021). Multi-phase seismic source imprint of tropical cyclones. *Nature communications*, *12*(1), 1–8.

Shapiro, N. M., Campillo, M., Stehly, L., & Ritzwoller, M. H. (2005). High-resolution surface-wave tomography from ambient seismic noise. *Science*, *307*(5715), 1615–1618.

Sieminski, A., Paulssen, H., Trampert, J., & Tromp, J. (2008). Finite-frequency sks splitting: measurement and sensitivity kernels. *Bulletin of the Seismological Society of America*, *98*(4), 1797–1810.

Tkalčić, H., Phạm, T.-S., & Wang, S. (2020). The earth's coda correlation wavefield: Rise of the new paradigm and recent advances. *Earth-Science Reviews*, 103285.

Tolman, H. L., et al. (2009). User manual and system documentation of wavewatch iii tm version 3.14. *Technical note, MMAB Contribution*, *276*, 220.

Wessel, P., Luis, J., Uieda, L., Scharroo, R., Wobbe, F., Smith, W., & Tian, D. (2019). The generic mapping tools version 6. *Geochemistry, Geophysics, Geosystems*, *20*(11), 5556–5564.

Wirth, E. A., & Long, M. D. (2014). A contrast in anisotropy across mid-lithospheric discontinuities beneath the central united states—a relic of craton formation. *Geology*, *42*(10), 851–854.

Yang, B. B., Liu, Y., Dahm, H., Liu, K. H., & Gao, S. S. (2017). Seismic azimuthal anisotropy beneath the eastern united states and its geodynamic implications. *Geophysical Research Letters*, *44*(6), 2670–2678.